Phase-controlled synthesis of iron phosphates via phosphation of β-FeOOH nanorods

CrystEngComm

PAPER

Phase-controlled synthesis of iron phosphates via phosphation of β-FeOOH nanorods†

Received 00th January 20xx,
Accepted 00th January 20xx

DOI: 10.1039/x0xx00000x

www.rsc.org/

Ronghe Lin,[a] Amol P. Amrute,[a] Frank Krumeich,[b] Károly Lázár,[c] Roland Hauert,[d] Maxim Yulikov[e] and Javier Pérez-Ramírez*[a]

Iron phosphates comprise an important class of materials with a wide range of applications. We have designed novel routes for the controlled synthesis of iron phosphate dihydrates of varying crystallographic phase (monoclinic and orthorhombic) and morphology. Our approach comprises the phosphation of β-FeOOH nanorods with aqueous phosphoric acid solutions. Through a systematic parametric study coupled to an array of characterisation techniques, including XRD, TEM, HAADF-STEM, AAS, N_2 sorption, TGA-MS, FTIR, UV-Vis, XPS, EXAFS, EPR, and ^{57}Fe Mössbauer spectroscopies, we unravel the complex synthesis chemistry both on macroscopic and microscopic levels. It is found that the formation of iron phosphates occurs exclusively under acidic conditions and in general involves the dissolution of β-FeOOH which, upon reaction with H_3PO_4, precipitates as $FePO_4{\cdot}2H_2O$. The pH of the treatment solution determines the crystallographic phase of the resulting product by regulating the rate of β-FeOOH dissolution and of the precipitation of the iron phosphates, while the treatment time is decisive for the preservation of the morphology. The formation of the monoclinic phase entails a fast iron dissolution and subsequent precipitation in the solution. The generation of the orthorhombic analogue involves an interfacial reaction between H_3PO_4 and β-FeOOH, forming an amorphous layer of iron phosphate, which crystallises into a pure phase with increasing treatment times. The thermal transformation of the hydrated to anhydrous iron phosphates is dependent on the phase and morphology of the precursors. The rod-shape of iron-rich orthorhombic $FePO_4{\cdot}2H_2O$ can be preserved even after annealing at 923 K, with the formation of mesopores. These novel nanostructures may widen the applications of iron phosphates and the routes developed herein can be anticipated to guide the fabrication of other metal phosphates.

1. Introduction

Iron phosphates are naturally existing minerals[1] and possess exceptional physical, chemical, and biocompatibility properties.[2-9] They have long been used in the steel and glass industries,[10,11] and are nowadays extensively applied in various fields like environmental purification,[12] biosensing,[13] ferroelectrics,[14] heterogeneous catalysis,[15-20] and lithium ion batteries.[21-24] Moreover, their crystal chemistry is rich due to the existence of their stable hydrated and anhydrous forms with different crystallographic phases (*e.g.*, monoclinic, orthorhombic, and with a tridymite structure ($P6_3/mmc$), etc.)[25-27] and their performances in catalysis and ion battery have been reported to correlate with these phases.[16,20,23,24] For instance, the orthorhombic $FePO_4$ is electrochemically two times more active than the monoclinic counterpart for lithium ion incorporation capacity.[23]

The hydrated iron phosphates are frequently used as precursors for the synthesis of $FePO_4$ by high-temperature annealing and $LiFePO_4$ by lithium intercalation.[7,28] Numerous preparation routes can be used to obtain the hydrated materials, such as sol-gel,[21,29,30] ion-exchange,[31] co-precipitation,[32,33] hydrothermal,[1,23,27] and microwave-assisted syntheses.[13] The main disadvantages of these methods are a low yield and limited control over the resulting crystallographic phase of the obtained solid. For example, the bottom-up approaches mentioned above almost exclusively lead to the formation of monoclinic $FePO_4{\cdot}2H_2O$. In seldom cases, the orthorhombic phase was also obtained. Whittingham *et al.* disclosed a hydrothermal route, starting from $FeCl_2$, LiCl, and H_3PO_4,[23] which resulted in a mixture of orthorhombic and monoclinic $FePO_4{\cdot}2H_2O$ phases. A more sophisticated method was developed by Tanaka and Taniguchi who started from the preparation of a complex layered iron phenyl phosphate $(Fe(OH)(C_6H_5PO_4H)_{1.6}(H_2PO_4)_{0.4}{\cdot}5.1H_2O)$.[34] Aging of this compound in an ammonia solution led to a slow crystallisation of monoclinic

[a] Institute for Chemical and Bioengineering, Department of Chemistry and Applied Biosciences, ETH Zurich, Vladimir-Prelog-Weg 1, CH-8093 Zurich, Switzerland. Email: jpr@chem.ethz.ch
[b] Laboratory of Inorganic Chemistry, Department of Chemistry and Applied Biosciences, ETH Zurich, Vladimir-Prelog-Weg 1, CH-8093 Zurich, Switzerland
[c] Department of Nuclear Analysis, Centre for Energy Research, MTA, Konkoly-Thege M. 29-33, H-1121 Budapest, Hungary.
[d] Empa, Swiss Federal Laboratories for Materials Science and Technology, Überlandstrasse 129, CH-8600 Dübendorf, Switzerland.
[e] Laboratory of Physical Chemistry, Department of Chemistry and Applied Biosciences, ETH Zurich, Vladimir-Prelog-Weg 2, CH-8093 Zurich, Switzerland.

† Electronic supplementary information (ESI) available: Characterisation of β-FeOOH-nr and selected samples derived from its phosphation by TEM, N_2 sorption, XRD, TGA-MS, FTIR, and UV-Vis. EPR spectra of reference $FePO_4$. Saturation index for the formation of orthorhombic $FePO_4{\cdot}2H_2O$ and α-Fe_2O_3. See DOI: 10.1039/x0xx00000x

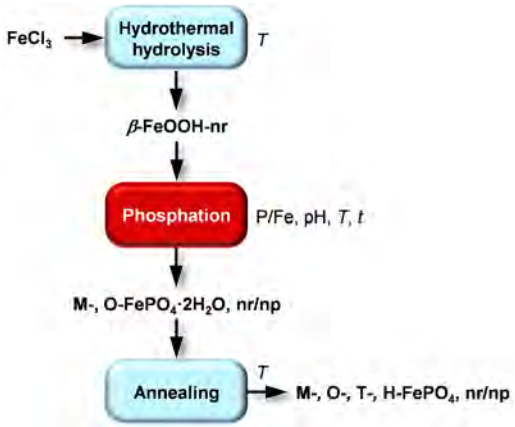

Fig. 1. Schematic of the novel synthetic route introduced herein, comprising: i) hydrothermal preparation of β-FeOOH nanorod (β-FeOOH-nr), followed by ii) its phosphation with H_3PO_4 into $FePO_4{\cdot}2H_2O$ of different phases and morphologies, and iii) annealing of the hydrated forms into various polymorphs of anhydrous $FePO_4$. The letters M, O, T, and H refer to the monoclinic, orthorhombic, tridymite, and hexagonal phases, respectively. The codes nr and np denote nanorod and nanoparticle morphology, respectively.

$FePO_4{\cdot}2H_2O$ and finally the orthorhombic form was achieved after 120 h with poor crystallinity. Masquelier *et al.*developed a more controlled method for the preparation of $FePO_4{\cdot}2H_2O$ with monoclinic, orthorhombic, and metastrengite phases by precipitation in diluted solutions.[35] However, the synthesis is time-consuming, requiring an aging step of several days, and the productivity is low because of the extremely low concentrations of iron and phosphorous precursors used. Besides, it is still unclear what leads to the crystallisation of $FePO_4{\cdot}2H_2O$ in distinct phases. Therefore, it is highly desirable to develop a more straightforward and versatile strategy for the controlled synthesis of hydrated iron phosphates and to gather a comprehensive understanding on the synthesis by unravelling the underlying chemistry.

Iron oxyhydroxides (FeOOH), with α-, β-, and γ-phases, are among the most common constituents of the Earth's crust. They play a crucial role in regulating the mobility of phosphates in natural aquatic and soil environments, as phosphate ions can be strongly bound to the surface of FeOOH. Intensive efforts have been devoted to the study of the interactions between PO_4^{3-} and FeOOH, covering a wide number of topics, such as phase and size effects of FeOOH,[35,36] the nature and conditions for the formation of iron phosphate on the surface,[36-38] and the surface adsorption models and mechanisms.[12,37,39-41] To our knowledge, there is no report on the intended synthesis of bulk iron phosphates from FeOOH.

Herein, we introduce a simple and scalable top-down strategy for the phase- and morphology-controlled synthesis of $FePO_4{\cdot}2H_2O$ *via* the phosphation of β-FeOOH nanorods (nr), synthesised *via* hydrothermal hydrolysis of $FeCl_3$ (Fig. 1). Subsequent annealing of the hydrated iron phosphates leads to different polymorphs of $FePO_4$. An array of characterisation techniques are employed to unravel the kinetics and mechanism of the crystallisation of $FePO_4{\cdot}2H_2O$ in different phases.

2. Experimental

Materials. β-FeOOH-nr were synthesised by the hydrolysis of iron chloride.[42,43] Briefly, cetyltrimethylammonium bromide (CTAB, 10 mmol, Sigma-Aldrich, purity >98%) was dispersed in 250 cm^3 deionised water and vigorously stirred for 30 min. To the resulting transparent solution, 25 mmol $FeCl_3{\cdot}6H_2O$ (Sigma-Aldrich, purity >99%) was added and stirred for another 30 min. The solution was transferred into a Teflon-lined stainless steel autoclave and heated at 353-413 K for 14 h. The solid was recovered by filtration, washed thoroughly with deionised water, and dried at 333 K under vacuum (30 mbar) for 12 h. For the synthesis of $FePO_4{\cdot}2H_2O$, β-FeOOH-nr powder (0.1 g) was added into a three-necked round flask containing 20 cm^3 H_3PO_4 aqueous solutions and refluxed at 353-413 K for 1-14 h. The nominal P/Fe molar ratio was adjusted by changing the concentration of H_3PO_4 (0.056-0.5 mol dm^{-3}), while the solid-to-solution ratio was kept constant (50 g β-FeOOH dm^{-3}). The precipitates were separated by filtration, washed thoroughly with deionised water, and dried at 373 K under vacuum (30 mbar) for 14 h. Anhydrous $FePO_4$ was prepared by the calcination of $FePO_4{\cdot}2H_2O$ in static air at 473-923 K for 5 h, with a ramp of 1 K min^{-1}.

Characterisation methods. Powder X-ray diffraction (XRD) was measured using a PANalytical X'Pert PRO-MPD diffractometer. Data were recorded in the 10-70° 2θ range with an angular step size of 0.017° and a counting time of 0.26 s per step. The iron content in both solids and filtrates after reflux treatments was analysed using a Varian SpectrAA 220FS atomic absorption spectrometer (AAS). Solids were digested with aqueous 36 wt.% HCl solution prior to measurements. The phosphorous content was determined by elemental analysis in a LECO CHN 900 combustion furnace. Nitrogen sorption at 77 K was performed using a Micromeritics 3Flex analyser. Prior to the measurements, the sample was evacuated to 10^{-1} mbar at 373 or 573 K for 3 h. Transmission electron microscopy (TEM) was measured using a FEI Technai F30 microscope operated at 300 kV. Samples were prepared by dipping the grid in a suspension of the solid in ethanol and drying in air. Scanning transmission electron (STEM) micrographs with a high-angle annular dark-field (HAADF) detector as well as elemental mappings with an energy-dispersive X-ray spectrometer (EDS) were acquired on a FEI Talos instrument operated at 200 kV. X-ray photoelectron spectroscopy (XPS) was performed on a Physical Electronics Quantum 2000 X-ray Photoelectron Spectrometer using monochromatic Al Kα radiation, generated from an electron beam operated at 15 kV and 32.2 W, and a hemispherical capacitor electron-energy analyser equipped with a channel plate and a position-sensitive detector. All spectra were shifted to the reference C 1*s* level of the carbon over-layer at 284.8 eV to compensate for any effect of sample charging. Elemental concentrations were analysed using the measured photoelectron peak areas after Shirley background subtraction and the built-in PHI sensitivity factors for calculation. Continuous wave electron paramagnetic resonance (EPR) spectra were recorded with a Bruker ELEXSYS E500 spectrometer operating at X band (microwave frequency 9.7-9.9 GHz), equipped with a super-high Q resonator (ER 4122 SHQ) and a He-flow cryostat (ESR 910, Oxford Instruments). Due to very large differences in the detected peak-to-peak

intensities for different samples, the room-temperature EPR spectra were recorded at 20 dB microwave attenuation (field modulation of 0.4 mT) for the samples with weaker EPR signals and 48 dB microwave attenuation (field modulation of 0.1 mT) for the samples with stronger EPR signals. Mössbauer spectra were collected at 77 and 300 K in a constant acceleration mode, using a Mössbauer spectrometer (KFKI-RegTron Co., Ltd.) with 1 GBq ^{57}Co/Rh source. Velocity calibration and isomer shifts were given relative to an absorber of metallic iron. Parameter fits were performed using a standard least-squares fitting routine with Lorentzian lines. The accuracy of shift parameters was *ca.* ±0.03 mm s^{-1}. The relative absorption data of the components were also calculated. X-ray absorption fine structure (XAFS) measurements at the Fe K-edge (7.12 keV) were carried out at the Super-XAS beamline at the Swiss Light Source (Villigen, Switzerland). The spectra were measured in transmission mode at room temperature. The EXAFS spectra were background corrected and normalised, and the resulting k^2 weighted spectra were processed by Fourier transform. Fourier transform infrared (FTIR) spectroscopy was performed using a Bruker Optics Vertex 70 spectrometer equipped with a high temperature cell, ZnSe windows, and a mercury-cadmium-telluride detector. The samples were mixed homogeneously with KBr with a weight ratio of 1:300 and pressed into discs. Spectra were recorded in the 400-4000 cm^{-1} range. UV-Vis spectroscopy was carried out using a Varian Cary 4000 spectrometer equipped with a diffuse reflectance cell (Harrick). Spectra were collected in the 200-800 nm range with a scanning rate of 150 nm min^{-1}. Thermogravimetric analysis (TGA) was performed using a Mettler Toledo TGA/DSC 1 Star microbalance connected to a Pfeiffer Vacuum Thermo-Star GDS 320 T1 mass spectrometer, after pre-treatment of the samples in air at 393 K for 2 h. The analysis was carried out in air (45 cm^3 STP min^{-1}), ramping the temperature from 393 to 1073 K at 5 K min^{-1}.

3. Results and discussion

3.1. Synthesis of β-FeOOH-nr

β-FeOOH-nr was synthesised by the hydrothermal hydrolysis of $FeCl_3$ at 333-413 K for 14 h. XRD analysis of the resulting solids revealed the formation of pure β-FeOOH at temperatures below 373 K, while at 393 K, both α-Fe_2O_3 and β-FeOOH coexisted and at 413 K, only α-Fe_2O_3 was present (Fig. S1). TEM images showed that the samples derived below 373 K have relatively uniform nanorod shapes with spindle-like tips (Fig. 2, Fig. S1). The average

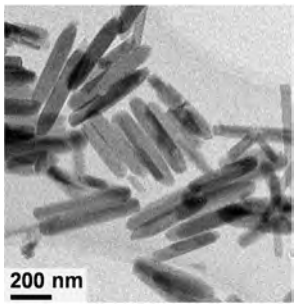

Fig. 2. TEM of β-FeOOH-nr crystals obtained by the hydrothermal hydrolysis of $FeCl_3$ at 373 K.

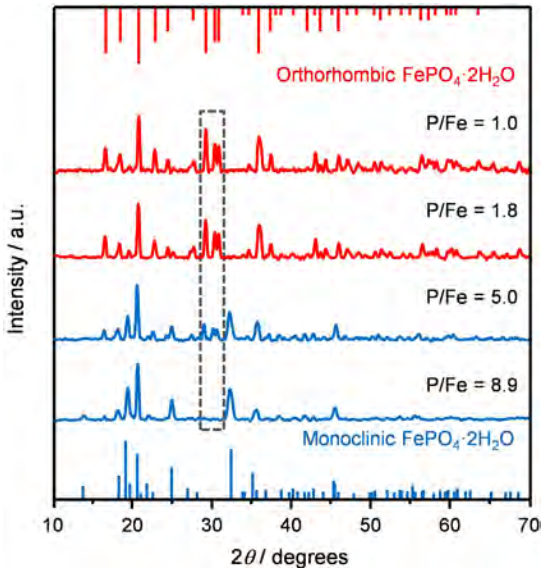

Fig. 3. XRD patterns of the solids obtained at different nominal P/Fe ratios *via* the phosphation of β-FeOOH with H_3PO_4 at 353 K for 14 h. Vertical lines on the top and bottom axes show the reference orthorhombic (JCPDS 33-667) and monoclinic (JCPDS 33-666) $FePO_4{\cdot}2H_2O$. Diffraction peaks of the orthorhombic phase gradually disappeared with increasing nominal P/Fe ratios, as indicated in the gray box.

dimensions and the total surface area of the nanorods synthesised at 373 K are 420×80 nm (estimated from 100 nanorods) and 16 m^2 g^{-1}, respectively.

3.2. Synthesis of $FePO_4{\cdot}2H_2O$

β-FeOOH-nr prepared at 373 K was employed as a novel precursor for the synthesis of iron phosphate dihydrate *via* phosphation using H_3PO_4. A systematic parametric study coupled to basic characterisations (XRD, AAS) was performed, leading to products of different phase and morphology. The key samples were deeply characterised to gain insights into the kinetics and mechanism of their formation.

3.2.1. Parametric study

The influence of the nominal P/Fe ratio (1.0-8.9) on the synthesis was evaluated at 353 K by keeping the volume-to-solid ratio constant. X-ray diffractograms of the obtained powders evidenced the formation of (*i*) orthorhombic $FePO_4{\cdot}2H_2O$ for P/Fe < 1.8, (*ii*) a mixture of both orthorhombic and monoclinic phases at 5.0, and (*iii*) the single monoclinic phase at 8.9 (Fig. 3). These results demonstrate that $FePO_4{\cdot}2H_2O$ can be directed into a particular phase by simply adjusting the nominal P/Fe ratio through our strategy. However, the latter quotient was tuned by varying the concentration of H_3PO_4 which also alters the pH of the treatment solution. Thus, the impact of pH was investigated through different comparative experiments (Fig. S2). The initial pH of the treatment solution in the nominal P/Fe = 1.8 was 1.5 and in P/Fe = 8.9, it was 1.2. In the first experiment, the latter pH value was achieved at P/Fe = 1.8 by adding HNO_3. The XRD pattern of the corresponding solid showed β-FeOOH as the dominant phase with a minor contribution from monoclinic $FePO_4{\cdot}2H_2O$. Strikingly, no diffraction

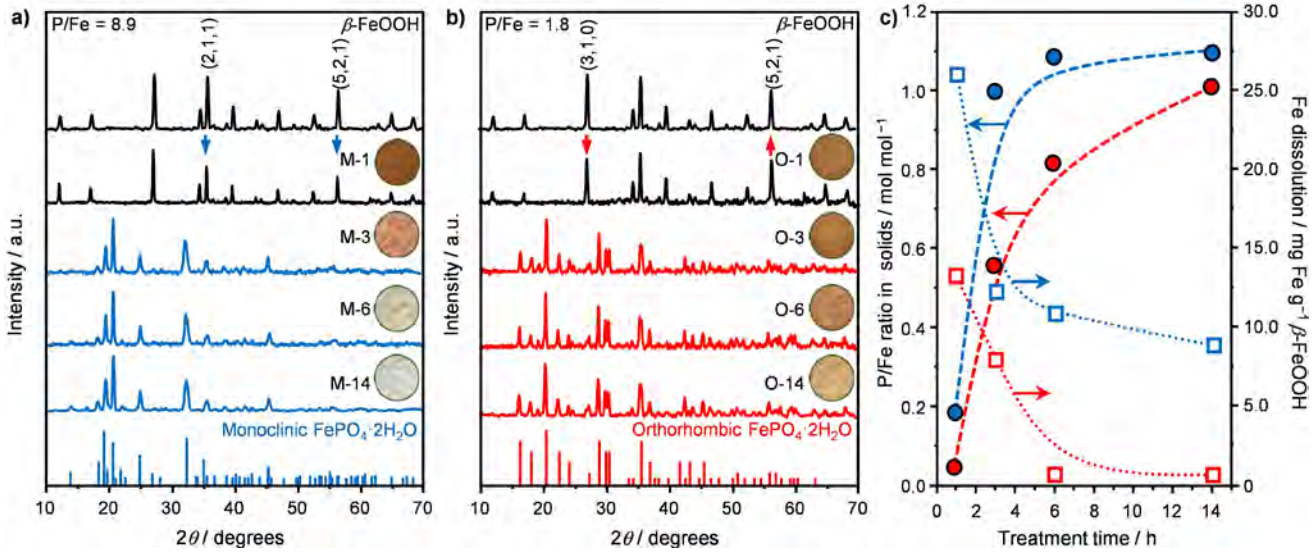

Fig. 4. Influence of the treatment time on the formation $FePO_4{\cdot}2H_2O$ *via* the phosphation of β-FeOOH-nr with H_3PO_4 at 353 K. **a,b**) XRD patterns of the solids (the M-*t* and O-*t* samples were derived with a nominal P/Fe atomic ratio of 8.9 and 1.8, respectively; where *t* denotes treatment time in hours). Inset: optical photographs of corresponding samples showing colour changes. **c**) P/Fe ratio in the solids and iron dissolution in the solution determined by AAS of the filtrate (P/Fe = 8.9: blue and P/Fe = 1.8: red). Vertical lines on the bottom axes in **a,b**) show the reference monoclinic (JCPDS 33-666) and orthorhombic (JCPDS 33-667) $FePO_4{\cdot}2H_2O$ phases. The arrows in **a,b**) indicate changes in the relative intensity of different crystal planes in M-1 and O-1 with respect to the β-FeOOH precursor.

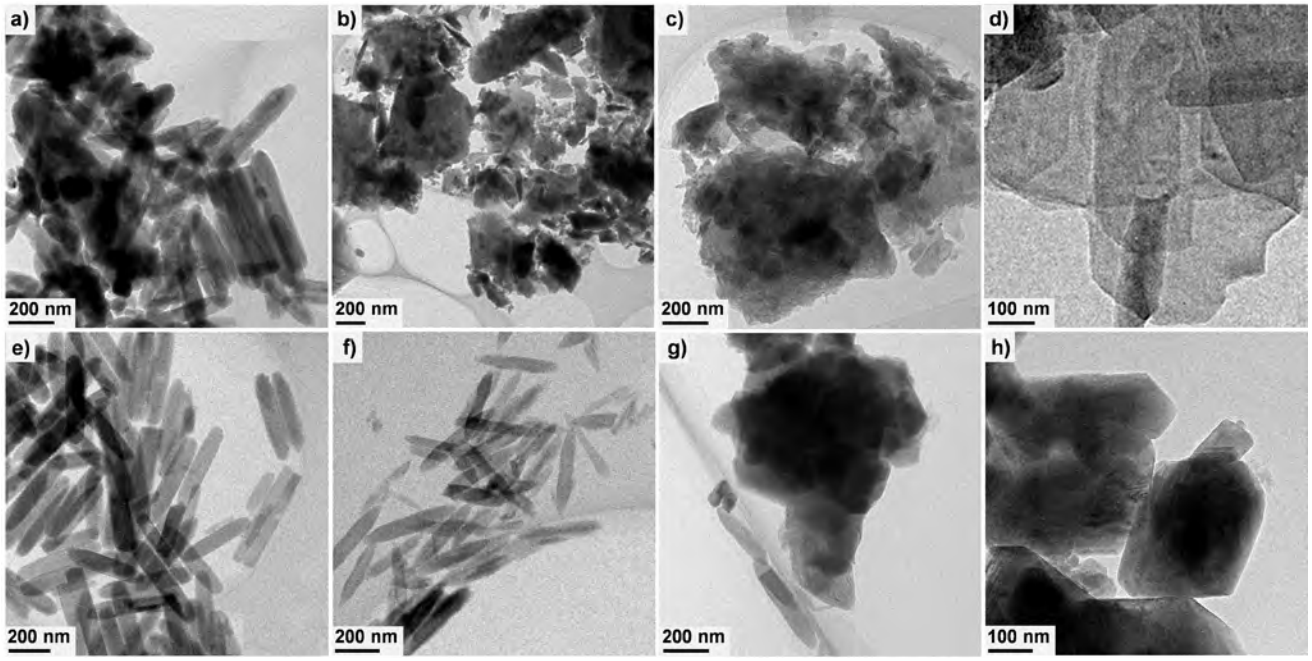

Fig. 5. TEM of the **a-d**) M-*t* and **e-h**) O-*t* samples obtained *via* the phosphation of β-FeOOH-nr with H_3PO_4 at 353 K at the nominal P/Fe = 8.9 and P/Fe = 1.8, respectively. *t* denotes treatment times of **a,e**) 1 h; **b,f**) 3 h; **c,g**) 6 h; and **d,h**) 14 h.

peaks of orthorhombic $FePO_4{\cdot}2H_2O$ were observed. Further experiments at P/Fe = 1.8 showed that no reactions occur under neutral or basic solution conditions. These results unequivocally suggest that (*i*) $FePO_4{\cdot}2H_2O$ can only be prepared under acidic conditions with this top-down approach and (*ii*) pH rather than the nominal P/Fe ratio of the treatment solution plays a crucial role in the crystallisation of $FePO_4{\cdot}2H_2O$ into different forms. Furthermore, a study of the impact of treatment temperature revealed that orthorhombic $FePO_4{\cdot}2H_2O$ forms selectively at P/Fe = 1.8, while only the monoclinic phase is attained at P/Fe = 8.9 between 353 and 413 K (Fig. S3), which indicates that the crystallisation mechanism is not sensitive to the temperatures studied.

To further explore the formation of $FePO_4{\cdot}2H_2O$ in a particular phase, the impact of the treatment time was studied at P/Fe ratios of 8.9 and 1.8. The obtained solids were denoted as M-*t* (P/Fe = 8.9) and O-*t* (P/Fe = 1.8), where *t* indicates the treatment time in hours.

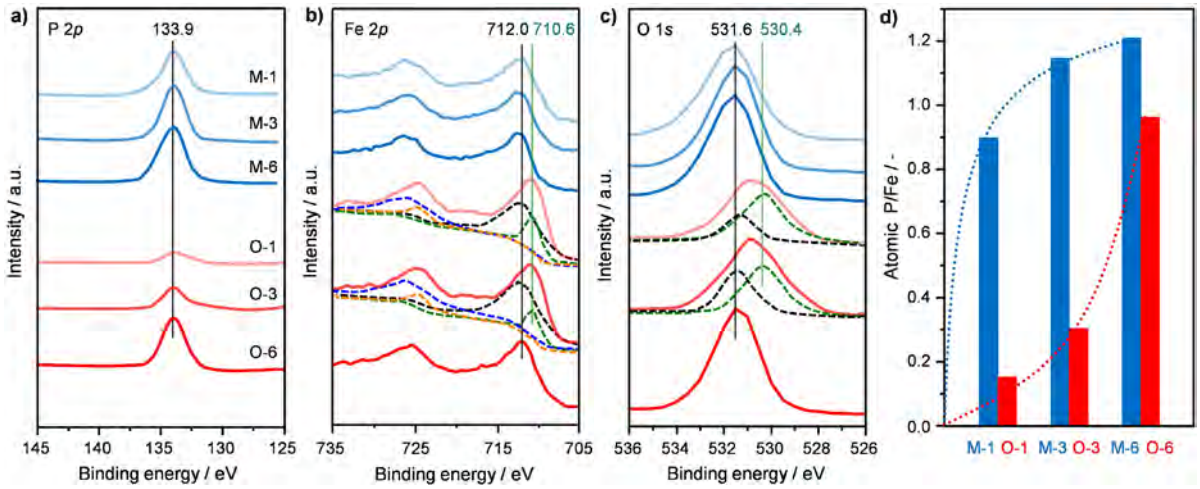

Fig. 6. a) P 2*p*, **b**) Fe 2*p*, and **c**) O 1*s* XPS spectra, and **d**) the surface P/Fe atomic ratios evidenced in the M-*t* and O-*t* samples derived from the time-dependent experiments. The dashed lines in **b**) and **c**) show the fitting results attained by peak deconvolution.

XRD analysis of the samples obtained after 1 h of treatment at both ratios exclusively evidenced the presence of the starting β-FeOOH, suggesting the absence of any significant amount of crystalline iron phosphate formation (Figs. 4a,b). Still, the interaction between β-FeOOH and H_3PO_4 can be reflected from the different relative intensities of the diffraction peaks. The (2,1,1) and (5,2,1) planes of β-FeOOH in M-1 were weakened, while in O-1 the latter was enhanced while the (3,1,0) plane was weakened. After 3 h of treatment, the diffraction peaks of β-FeOOH disappeared and reflections corresponding to the monoclinic and orthorhombic $FePO_4{\cdot}2H_2O$ were formed at P/Fe = 8.9 and 1.8, respectively. A further increase of the treatment time resulted in similar XRD patterns in both cases. However, the optical photographs of the samples (insets in Figs. 4a,b) showed stark colour changes from dark-brown to white for the M-*t* samples, indicating an increase of the P/Fe ratio in the solids. Contrarily, such colour changes occurred more gradually in the case of the O-*t* samples, suggesting a slower conversion of β-FeOOH to the orthorhombic $FePO_4{\cdot}2H_2O$. This is further revealed from the P/Fe ratio in the solids after each treatment (Fig. 4c). The M-*t* samples displayed much higher P/Fe ratios at all treatment times and also reached a value of 0.98 (*i.e.* close to stoichiometry of iron phosphate) much faster (within 3 h) than the O-*t* analogues, which required 14 h to attain a similar P/Fe (Fig. 4c, solid symbols). This hints a faster rate of iron phosphate formation at P/Fe = 8.9 than at 1.8 which is likely related to the higher availability of PO_4^{3-} ions in the former case.

Finally, the impact of the iron precursor was examined by replacing the β-FeOOH-nr with $Fe(NO_3)_3$, and as expected only monoclinic $FePO_4{\cdot}2H_2O$ resulted upon prolonged treatment (Fig. S2). This evidenced the unique role of β-FeOOH-nr in the formation of the orthorhombic $FePO_4{\cdot}2H_2O$.

3.2.2. Characterisation of selected samples

In-depth understanding of the bulk and surface properties of the samples obtained after phosphation of β-FeOOH-nr at nominal P/Fe = 1.8 or 8.9 for different times was attained through characterisation by TEM, XPS, EPR, EXAFS, and ^{57}Fe Mössbauer spectroscopies.

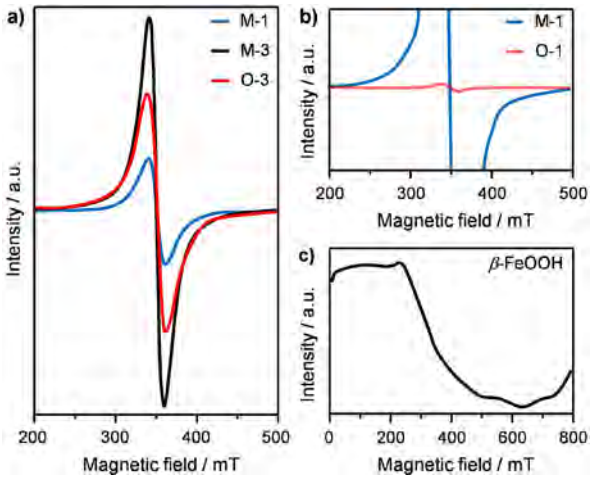

Fig. 7. Room-temperature EPR spectra of selected M-*t* and O-*t* samples and of β-FeOOH-nr at **a,c**) 48 dB microwave attenuation (0.1 mT field modulation amplitude) and **b**) 20 dB microwave attenuation (0.4 mT field modulation amplitude).

M-*t* samples. The changes in the morphology of β-FeOOH-nr upon phosphation were studied by electron microscopy (Figs. 5a-d). The nanorod shape was generally retained after 1 h of treatment, with some particle aggregation (Fig. 5a). After 3 h, the nanorod morphology was completely transformed into particles of irregular shapes (Fig. 5b). This severe alteration of the morphology is most likely related to the fast dissolution of β-FeOOH (*vide infra*). For the samples after 6 and 14 h, the particle agglomeration seemed to be very pronounced resulting in huge aggregates (~ 0.5 μm) of $FePO_4{\cdot}2H_2O$ with plate-like morphology (Figs. 5c,d).

Surface compositions were analysed by XPS. The P 2*p*, Fe 2$p_{3/2}$, and O 1*s* spectra of all the M-*t* samples centred at binding energies of 133.9, 712.0, and 531.6 eV (Figs. 6a-c), respectively, which match well with those previously reported for iron phosphates.[44] EPR spectra of the M-1 and M-3 samples showed an EPR resonance around the proportionality factor (*g*-factor) of ~ 2 (Fig. 7a), which increased in intensity with time. These resonance patterns were

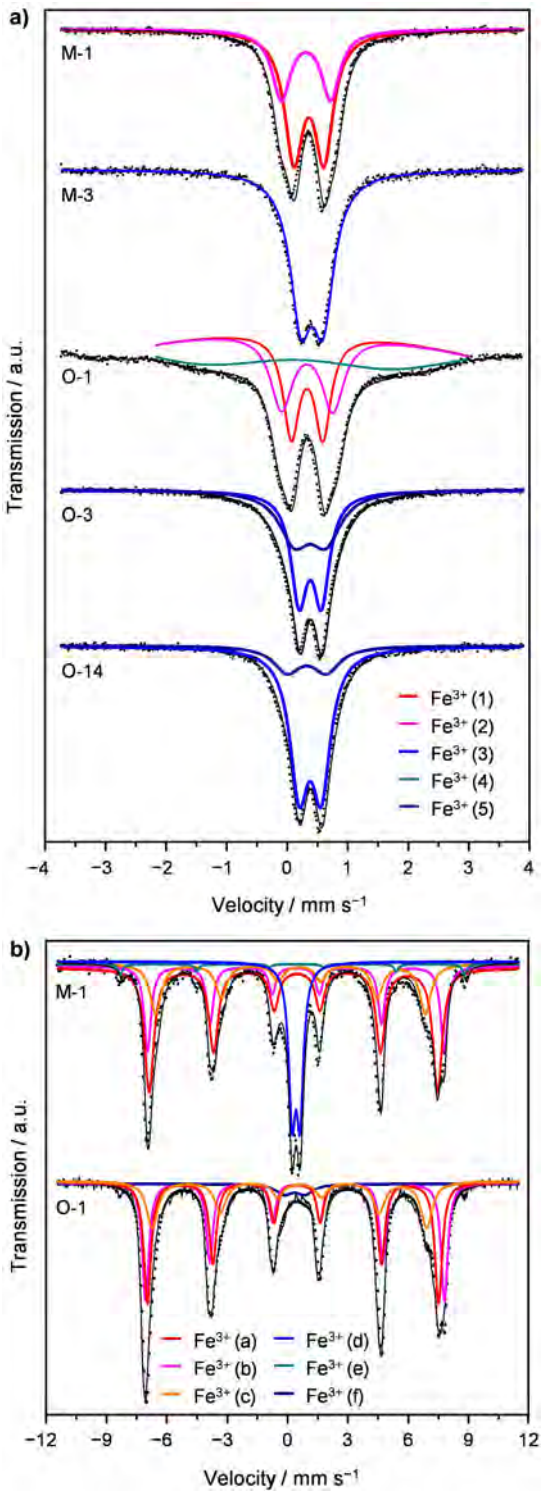

Fig. 8. ^{57}Fe Mössbauer spectra of the M-*t* and O-*t* samples at **a**) 300 K and **b**) 77 K. Black dots: experimental data; black lines: fitted spectra; colour lines: least-square fits showing different iron components.

absent in the EPR spectrum of β-FeOOH (Fig. 7c) and were similar to that obtained for $FePO_4$ (Fig. S4).[45] These results unequivocally evidence the presence of iron phosphate in all the M-*t* samples. Interestingly, although XRD exclusively showed the presence of β-FeOOH in M-1, it appears that its surface contains $FePO_4{\cdot}2H_2O$ already in 1 h.

The nature of the surface iron phosphates formed after short treatment times in the M-*t* samples, whether amorphous or crystalline, remains unclear. Thus, Mössbauer spectroscopy was applied to distinguish different iron species in these samples. Room-temperature (RT) ^{57}Fe Mössbauer spectra of the M-1 and M-3 samples are presented in Fig. 8a. The deconvolution of Mössbauer spectrum of M-1 leads to two doublets. The isomer shift (δ) and electric quadrupole splitting (Δ) derived from these doublets indicate the presence of two Fe^{3+} components of β-FeOOH (Table 1), in line with results reported elsewhere.[46,47] RT spectrum of M-3 was composed of only one Fe^{3+} component, whose δ and Δ values match to those for crystalline $FePO_4{\cdot}2H_2O$.[46] These outcomes are in agreement with XRD results. Liquid nitrogen temperature (LNT) ^{57}Fe Mössbauer spectrum of M-1 was recorded to gain more details on iron components (Fig. 8b and Table 1). At LNT, this sample displayed magnetic behaviour. The δ and Δ values suggest β-FeOOH as the main phase, in line with RT spectrum. In addition, the existence of iron phosphates was unravelled (component Fe^{3+} (d)),[46] corroborating the XPS and EPR findings. A relatively small FWHM value of Fe^{3+} (d) suggests the crystalline nature of this phase.

O-*t* samples. TEM images of the O-*t* samples showed a different behaviour compared to those of the M-*t* analogues (Figs. 5e-h). The nanorod shape of β-FeOOH remained relatively intact for O-1 and O-3. Even after 6 h (*i.e.* O-6), some rod-shaped particles could still be observed. O-14 displayed a marked particle agglomeration. Thus, these results highlight the stability differences of β-FeOOH-nr under the various treatment conditions.

The P2*p*, Fe2*p*, and O1*s* XPS spectra of the O-*t* samples are quite different from those of the M-*t* ones (Figs. 6a-c). First, for the P 2*p* spectra, the intensity of the peaks at 133.9 eV increased progressively with the treatment time, demonstrating the gradual enrichment of phosphates on the surface. Secondly, the Fe 2*p* and O 1s spectra showed a clear shift to lower binding energies for the 1 and 3 h samples (O-1 and O-3). Deconvolution of these peaks indicates the presence of two surface compositions: (*i*) iron phosphates (Fe $2p_{3/2}$ at 712.0 eV and O 1*s* at 531.6 eV) and (*ii*) β-FeOOH (Fe $2p_{3/2}$ at 710.6 eV and O 1*s* at 530.4 eV).[44,48] The phosphate contribution on the surface increased with time and reached 100% after 6 h. These observations are also supported by EPR spectra of O-1 and O-3 (Fig. 7a,b), which further confirmed the gradually strengthening EPR signals for iron phosphates with increasing treatment time.

RT ^{57}Fe Mössbauer spectra of the O-*t* samples are presented in Fig. 8a. The deconvolution of Mössbauer spectrum of O-1 leads to three doublets. Two of them (Fe^{3+} (1) and Fe^{3+} (2)) showed similar δ and Δ values to those of β-FeOOH, while the additional component (Fe^{3+} (4)) exhibited magnetic splitting. This difference might originate from the preferential growth of different crystal planes of β-FeOOH (Figs. 4a,b). LNT spectrum of O-1 displayed more prominent magnetic behaviour (Fig. 8b and Table 1). Three sextets related to β-FeOOH were obtained by deconvolution. An additional component (Fe^{3+} (f)) can be ascribed to iron phosphate, with similar

Table 1. ^{57}Fe Mössbauer parameters of the M-*t* and O-*t* samples at 77 and 300 K.

Sample code	Composition	Component	δ^a (mm s^{-1})	Δ^b (mm s^{-1})	FWHM^c (mm s^{-1})	MHF^d (Tesla)	F^e (%)
M-1	β-FeOOH	Fe^{3+} (1)	0.38	0.48	0.35	-	65
	β-FeOOH	Fe^{3+} (2)	0.37	0.91	0.34	-	35
M-3	Crystalline $FePO_4{\cdot}2H_2O$	Fe^{3+} (3)	0.44	0.37	0.43	-	100
O-1	β-FeOOH	Fe^{3+} (1)	0.37	0.53	0.33	-	-
	β-FeOOH	Fe^{3+} (2)	0.37	0.94	0.40	-	-
	β-FeOOH (magnetic)^f	Fe^{3+} (4)	-	-	-	-	-
O-3	Crystalline $FePO_4{\cdot}2H_2O$	Fe^{3+} (3)	0.43	0.36	0.31	-	52
	Amorphous $FePO_4{\cdot}2H_2O$	Fe^{3+} (5)	0.40	0.66	0.67	-	48
O-14	Crystalline $FePO_4{\cdot}2H_2O$	Fe^{3+} (3)	0.42	0.37	0.35	-	79
	Amorphous $FePO_4{\cdot}2H_2O$	Fe^{3+} (5)	0.39	0.81	0.50	-	21
M-1^g	β-FeOOH	Fe^{3+} (a)	0.47	0.20	0.45	44.2	33
	β-FeOOH	Fe^{3+} (b)	0.46	0.42	0.72	41.2	24
	β-FeOOH	Fe^{3+} (c)	0.48	-	0.33	45.7	17
	Crystalline $FePO_4{\cdot}2H_2O$	Fe^{3+} (d)	0.52	0.39	0.43	-	23
	α-Fe_2O_3	Fe^{3+} (e)	0.43	-	0.28	52.9	2
O-1^g	β-FeOOH	Fe^{3+} (a)	0.47	0.21	0.41	44.6	37
	β-FeOOH	Fe^{3+} (b)	0.45	0.48	0.66	41.9	26
	β-FeOOH	Fe^{3+} (c)	0.48	0.06	0.36	46.1	32
	Amorphous $FePO_4{\cdot}2H_2O$	Fe^{3+} (f)	0.48	1.02	1.10	-	5

^{a}Isomer shift. ^{b}Electric quadrupole splitting. ^{c}Full linewidth at half maximum. ^{d}Mean hyperfine magnetic field. ^{e}Relative resonance areas of different components of the absorption patterns. ^{f}Component exhibiting magnetic relaxation at 300 K, therefore no accurate data could be provided. ^{g}Spectra were collected at 77 K. Most of FWHM values are within 0.28-0.50 mm s^{-1}, close to the natural line width of iron in a perfect crystalline lattice, *i.e.*, 0.19-0.25 mm s^{-1}, demonstrating the reliability of the fitting results.

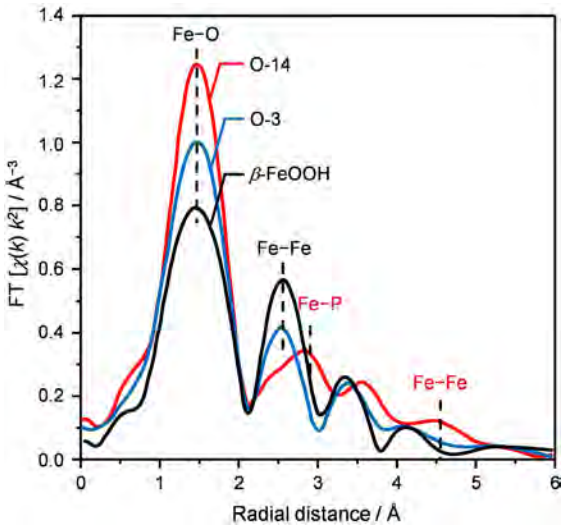

Fig. 9. k^2-weighted Fourier transform EXAFS spectra of the β-FeOOH-nr, O-3, and O-14 (not phase-corrected).

δ values to that of the crystalline iron phosphates (Fe^{3+} (d)), but with a much larger Δ value. The latter is likely because of the formation of amorphous iron phosphates on the surface, which cause more local defects as revealed by the larger FWHM of Fe^{3+} (f). The RT spectrum of O-3 indicated two iron species (Table 1), one of which (*i.e.*, Fe^{3+} (3)) led to similar δ and Δ values to those of M-3, suggesting the existence of crystalline $FePO_4{\cdot}2H_2O$ also in O-3. The other doublet in O-3 disclosed a similar δ value but relatively higher Δ, which points to the presence of amorphous iron phosphates.[45] O-14 revealed similar Mössbauer footprints as those of O-3 (Table 1), indicating that this sample contains the same iron species. However, the relative resonance area (*F*) of crystallised $FePO_4{\cdot}2H_2O$ in O-14 was significantly higher as compared to that in O-3, which evidences the amorphous to crystalline transformation of $FePO_4{\cdot}2H_2O$ with prolonged treatment time.

The presence of β-FeOOH in the O-3 sample, as evidenced by XPS, was further confirmed by EXAFS study. The Fourier transform EXAFS spectra of O-3, O-14, and β-FeOOH-nr were recorded (Fig. 9). Peaks located at ~1.5, 2.5, and 2.8 Å were attributed to the Fe–O, Fe–Fe, and Fe–P interactions, respectively.[46] The peaks at 2.8 and 4.6 Å (typical for the Fe–P and Fe–Fe interactions, respectively, in iron phosphates[46]) are absent for O-3, while they are observed in the spectrum of O-14. This is probably due to the better crystallinity of iron phosphates in the latter, in line with Mössbauer results. In addition, O-3 and β-FeOOH resulted in peaks at similar positions, indicating that these two samples possess a similar structure. Still, the influence of H_3PO_4 treatment on β-FeOOH-nr is reflected by a reduced intensity of the second major peak of O-3. This is in line with the XPS analysis and supports the existence of β-FeOOH in O-3. The absence of the latter phase in the X-ray diffractogram suggests that it is only present at the surface or is amorphous.

Overall, the above characterisation results demonstrate that the generation of monoclinic $FePO_4{\cdot}2H_2O$ involves a faster phosphation of β-FeOOH-nr, with a rapid morphological change into nanoparticles. In contrast, the formation of orthorhombic $FePO_4{\cdot}2H_2O$ occurs in a more controlled manner: amorphous iron phosphate first formed on the surface and subsequently crystallised into the orthorhombic phase. This also preserves the rod-shape of the precursor for a longer treatment duration.

3.3. Thermodynamic and kinetic analysis

A simplified model considering the β-FeOOH-nr-H_3PO_4 system was developed (Fig. S5) for providing a rough thermodynamic prediction for the formation of orthorhombic $FePO_4{\cdot}2H_2O$ *versus* α-Fe_2O_3. A saturation index (SI) is introduced (Eq. 1):

$$SI = \log IAP - \log K_{sp} \quad (1)$$

where IAP and K_{sp} are the ion activity product and solubility product constants, respectively. A positive SI value confirms the thermodynamic feasibility of the formation of a particular phase. Thus, the model suggests that the generation of orthorhombic $FePO_4{\cdot}2H_2O$ is thermodynamically possible in a wide pH range (0.5-9). However, the formation of α-Fe_2O_3 dominates above an SI value of 2.5, thus limiting the pH for orthorhombic $FePO_4{\cdot}2H_2O$ formation to below 1.6. This matches well with our experimental findings (Fig. S2) that iron phosphate formation occurs exclusively under acidic conditions. Therefore, kinetic control seems to be more crucial than thermodynamic for the successful synthesis of orthorhombic $FePO_4{\cdot}2H_2O$.

The kinetics of the formation of the monoclinic and orthorhombic phases can be estimated from the respective iron dissolution profiles (Fig. 4c, open symbols). Faster iron dissolution was determined at the beginning of the treatment, which progressively dropped with increasing times in both cases. This result indicates that the general transformation from β-FeOOH to $FePO_4{\cdot}2H_2O$ first involves the dissolution of iron, followed by the precipitation/deposition in the solution or at the interface (Eq. 2):

$$\beta\text{-FeOOH} \rightarrow Fe^{3+} \rightarrow FePO_4{\cdot}2H_2O \quad (2)$$

where the rates of iron dissolution and iron phosphate formation are denoted by k_1 and k_2, respectively. During the synthesis of the M-*t* samples, the iron was always detected in the filtrate in a significant amount, suggesting a faster dissolution of β-FeOOH-nr compared to the precipitation into iron phosphate. However, the preparation of the O-*t* samples unravels that the iron content in the filtrate was much lower and almost undetectable after 6 h, signifying that the dissolution and precipitation might reach an equilibrium by this time. Thus, it appears that the dissolution and precipitation rates determine the phase and morphology of the formed $FePO_4{\cdot}2H_2O$. A slower reaction between β-FOOH and H_3PO_4 leads to the orthorhombic phase, while a faster reaction (at elevated H_3PO_4 concentration or pH < 1.2) causes the formation of monoclinic analogue. This is supported by the characterisation methods described above (Section 3.2.2.). Analysis of the surface P/Fe ratio by XPS revealed a faster increase of P on the surface of the M-*t* than on the O-*t* samples (Fig. 6d). EPR and Mössbauer spectroscopy also unambiguously pointed to the much enhanced formation rates of iron phosphates in the M-*t* than in O-*t* samples. Besides, a slower reaction rate also preserved the nanorod morphologies up to 6 h treatment time in the O-*t* samples as evidenced by TEM analysis (Fig. 5).

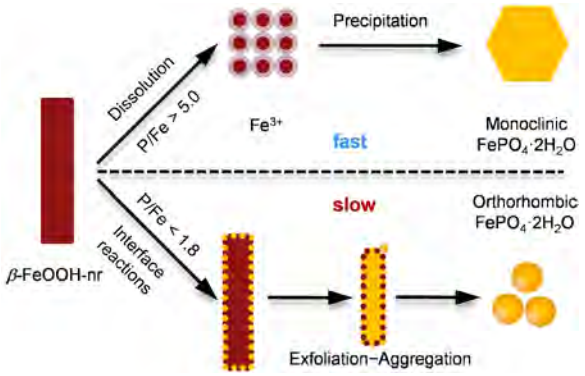

Fig. 10. Mechanisms of the formation of monoclinic and orthorhombic $FePO_4{\cdot}2H_2O$ with different morphology by the phosphation of β-FeOOH-nr with H_3PO_4. The monoclinic phase with a layered structure was formed by a fast dissolution-precipitation process. The formation of orthorhombic form involved a slow interfacial reaction on the nanorods, generating first amorphous iron phosphates on the surface that gradually crystallised into the orthorhombic phase, with the preservation of the rod structure. The final particles might be formed *via* aggregation of exfoliated iron phosphates from the nanorods.

3.4. Mechanism of $FePO_4{\cdot}2H_2O$ formation

Previous efforts towards the synthesis of orthorhombic $FePO_4{\cdot}2H_2O$ were quite unsuccessful. The hydrated iron phosphates are usually prepared by solution chemistry and the monoclinic phase is most commonly formed. Besides, the transformation between these two phases has already been reported, but remains inconclusive. For example, Whittingham *et al.* claimed that a mixture of orthorhombic and monoclinic $FePO_4{\cdot}2H_2O$ will transform into a pure monoclinic form with prolonged time in a hydrothermal synthesis.[23] In contrast, Tanaka and Taniguchi reported the reverse conversion from monoclinic to orthorhombic with increasing aging time.[34] Our results shed light on the phase-selective formation of $FePO_4{\cdot}2H_2O$ through kinetic control. The different rates of iron dissolution and iron phosphate precipitation (k_1 and k_2 in Eq. 2) might lead to diverse nucleation routes. This is in line with the fact that distinct interactions between β-FeOOH-nr and H_3PO_4 were evidenced during the formation of monoclinic and orthorhombic $FePO_4{\cdot}2H_2O$ (FTIR, Fig. S6 and UV-Vis Fig. S7). For the former phase, the higher iron dissolution and faster overall transformation rates could cause the precipitation of iron phosphates in the solution. This is in line with XPS analysis, indicating iron phosphates as the only surface composition during the formation of the monoclinic form. On the contrary, the orthorhombic phase formed much more slowly at a lower P/Fe ratio with less iron dissolution, which favours the nucleation at the interface rather than in solution. This is strongly supported by the surface compositions determined by XPS, testifying the coexistence of β-FeOOH and iron phosphates on the surface of O-1 and O-3, and by TEM, showing the preservation of nanorod structures (O-3 and O-6). The resulting iron phosphates were initially amorphous in nature, and gradually transformed to

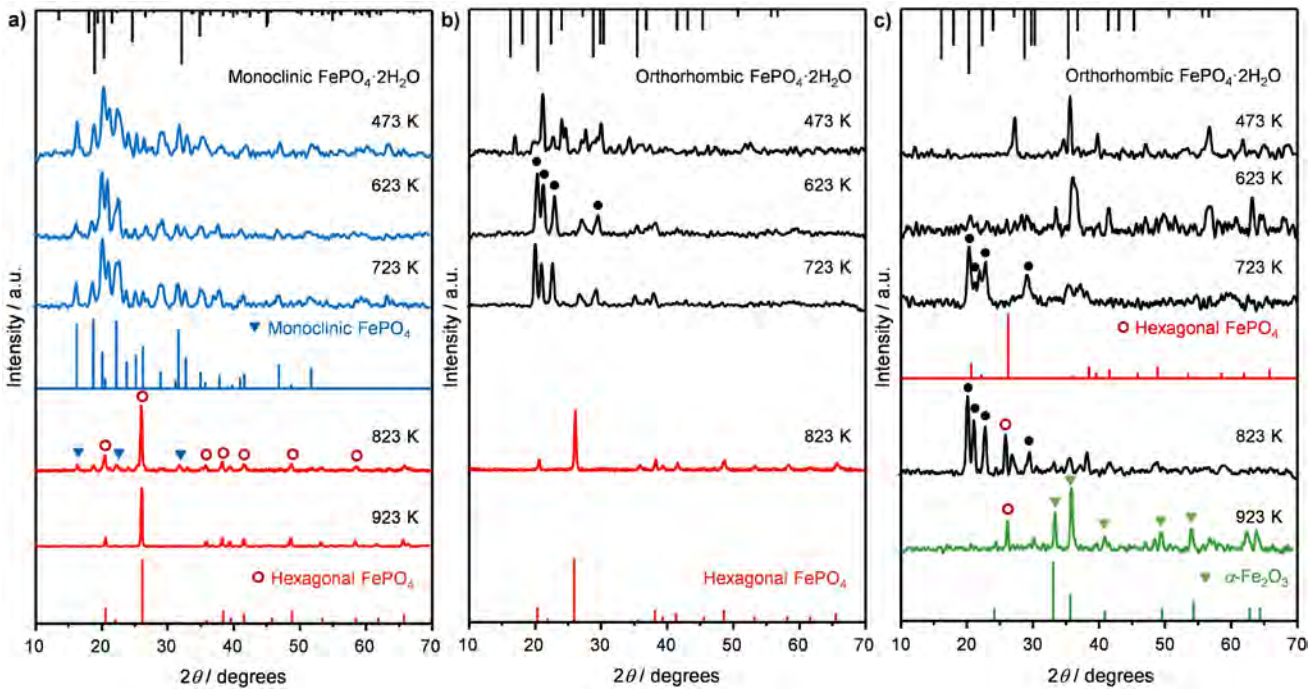

Fig. 11. XRD patterns of the **a**) M-3, **b**) O-14, and **c**) O-3 samples annealed at different temperatures. Vertical lines in the graphs show the reference monoclinic (JCPDS 33-666) and orthorhombic (JCPDS 33-667) $FePO_4·2H_2O$, monoclinic (JCPDS 56-0140) and hexagonal (JCPDS 84-0876) $FePO_4$, and α-Fe_2O_3 (JCPDS 33-0664). ● denotes tridymite $FePO_4$.

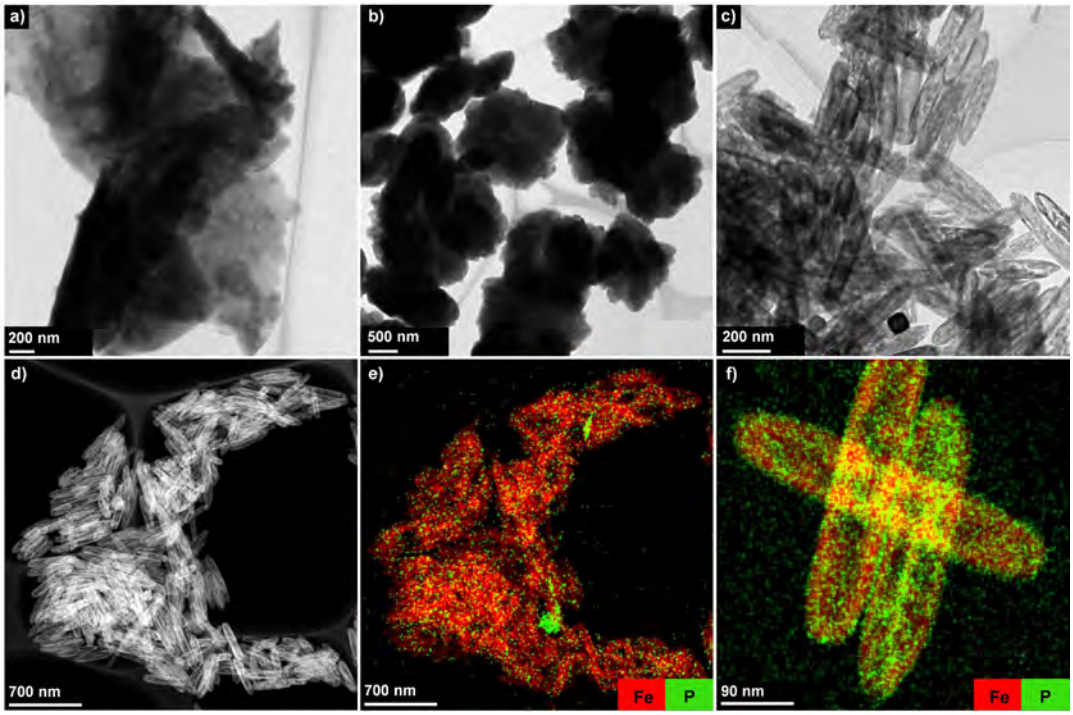

Fig. 12. TEM of **a**) M-3 calcined at 923 K, **b**) O-14 calcined at 823 K, and **c**) O-3 calcined 923 K. **d**) HAADF-STEM and **e,f**) elemental mapping of O-3 calcined at 923 K.

the orthorhombic phase, as evidenced by both Mössbauer spectroscopy and EXAFS. Based on these evidences, a possible mechanism for the phase-specific synthesis of iron phosphates by phosphation of β-FeOOH-nr with H_3PO_4 is proposed (Fig. 10).

3.5. From hydrated to anhydrous iron phosphates

3.5.1. Thermal stability and phase evolution

The dehydration behaviour of the as-synthesised monoclinic and orthorhombic $FePO_4·2H_2O$ (M-3, O-14, and O-3) was studied by TGA-MS (Fig. S8). The decomposition of the β-FeOOH-nr precursor

was compared for reference. The thermal stabilities of both the M-3 and O-14 samples were quite similar. A sharp weight loss of *ca*. 20%, equivalent to that expected for the conversion of $FePO_4{\cdot}2H_2O$ to $FePO_4$, due to the removal of H_2O (see MS signals in Fig. S8) was observed in a narrow temperature range of 400-420 K. O-3 also exhibited a rapid weight loss in 400-420 K region, but displayed a tailing up to 800 K, which resembles that recorded for β-FeOOH-nr. This is basically because of the presence of β-FeOOH in the O-3 sample, as demonstrated by the characterisation results (*vide supra*). Overall, the hydrated forms can be converted into anhydrous by annealing above 450 K.

Thus, based on TGA results, the phase evolution of M-3, O-3, and O-14 was investigated in the temperature range of 473-923 K (Fig. 11). For the M-3 sample, the monoclinic $FePO_4{\cdot}2H_2O$ was readily converted into monoclinic $FePO_4$ at 473 K (Fig. 11a). This phase remained stable up to 823 K, the temperature at which hexagonal $FePO_4$ coexisted. Further increase of the calcination temperature to 923 K led to a pure hexagonal $FePO_4$. Annealing of the O-14 sample at 473 K resulted in orthorhombic $FePO_4$.[35] Calcination at 623 K transformed O-14 into another phase that adopted the so-called tridymite structure.[35] Pure hexagonal $FePO_4$ was formed at 823 K with the complete collapse of the tridymite structure. Heating of O-3 led to even more complex structures, especially when the calcination temperature was below 723 K, likely due to the multi-component nature of this sample. Tridymite phase was found at 723-823 K and the hexagonal form appeared at 823 K, while at 923 K, dominant diffraction peaks of α-Fe_2O_3 were observed. The formation of both tridymite and α-Fe_2O_3 was delayed by at least 100 K for O-3 as compared to O-14 and β-FeOOH-nr (Fig. S9), respectively, possibly due to the interactions between iron phosphates and β-FeOOH.

3.5.2. Morphology and porosity

The textural properties of the M-3, O-3, and O-14 samples after high temperature annealing were evaluated by N_2 sorption and electron microscopy. The total surface areas of pure hexagonal $FePO_4$ obtained by the calcination of M-3 at 923 K and O-14 at 823 K were 4 and 3 $m^2\,g^{-1}$, respectively, suggesting a severe aggregation of the particles during heat treatment. This was corroborated by TEM images (Figs. 12a,b). The aggregation for M-3 at 923 K appeared to originate from the coupling of plate-like structures in a planar dimension. A quite different morphology was found for O-14 calcined at 823 K, which was composed of randomly arranged particles. In contrast to the calcined M-3 and O-14 samples, O-3 after calcination at 823 K and 923 K exhibited a higher surface area of 21 and 18 $m^2\,g^{-1}$, respectively. TEM image of O-3 calcined at 923 K revealed a relatively homogeneous and porous nanorod morphology with dimensions similar to the precursor (Fig. 12c). The porosity was further confirmed by N_2 sorption (Fig. S10). The generation of pores could be ascribed to the dehydration and combustion of residual CTAB during annealing process (Fig. S8). Elemental mapping on the selected area in the HAADF image evidenced an even distribution of Fe and P, with higher density of Fe (Figs. 12d,e). Besides, the enrichment of P in some small particles can be observed. A higher magnification image unambiguously disclosed the porous nature and the coexistence of both Fe and P species on the surface of this sample (Fig. 12f).

4. Conclusions

In this contribution, we have developed a novel top-down method for the controlled synthesis of $FePO_4{\cdot}2H_2O$ with different phase and morphology, employing the phosphation of β-FeOOH-nr with H_3PO_4. The key is the choice of a well-defined solid (β-FeOOH-nr) as an iron precursor, enabling the quantification of dissolved iron species during the treatment, the examination of morphological alterations, and the extent of transformation into phosphate forms caused by the reaction with H_3PO_4. A battery of characterisation methods was applied to unveil the chemistry of iron phosphate formation. It is demonstrated that the crystallographic nature and the morphology of hydrated iron phosphates strongly depended on the kinetics of the iron dissolution and iron phosphate formation, which in could be controlled by varying the pH or the nominal P/Fe ratio of the treatment solutions. Monoclinic $FePO_4{\cdot}2H_2O$ crystals with a layered structure were formed in more acidic solutions with a faster iron dissolution rate, followed by their precipitation in the solution. The formation conditions of orthorhombic $FePO_4{\cdot}2H_2O$ were much milder. It first involved the reaction on the surface of β-FeOOH-nr, forming an amorphous phosphates layer. Subsequent exfoliation, followed by aggregation led to orthorhombic $FePO_4{\cdot}2H_2O$ particles of several microns. Calcination treatments of $FePO_4{\cdot}2H_2O$ above 473 K led to the formation of anhydrous forms with different phases, which was dependent on the initial phase and annealing temperature applied. We believe that these findings will guide the prospective synthesis of other metal phosphates.

Acknowledgements

The Electron Microscopy Centre of ETH Zurich (ScopeM) is acknowledged for the use of their facilities. We are indebted to Dr. O. Safonova for providing assistance with the XAS measurements. The Micromeritics Grant Program is thanked for the award of the 3Flex instrument. Dr. S. Mitchell is acknowledged for comments on the manuscript.

References

1 C. Trobajo, A. Espina, E. Jaimez, S. A. Khainakov and J. R. Garcia, *J. Chem. Soc., Dalton Trans.,* 2000, **5**, 787.
2 C. A. Boras, R. Romagnoli and R. O. Lezna, *Electrochim. Acta,* 2000, **45**, 1717.
3 M. S. Whittingham, *Chem. Rev.,* 2014, **114**, 11414.
4 M. Pramanik, Y. Tsujimoto, V. Malgras, S. X. Dou, J. H. Kim and Y Yamauchi, *Chem. Mater.,* 2015, **27**, 1082.
5 M. Pramanik, M. Imura, J. Lin, J. Kim, J. H. Kim and Y. Yamauchi, *Chem. Commun.,* 2015, **51**, 13806.
6 F. Omenya, N. A. Chernova, R. Zhang, J. Fang, Y. Huang, F. Cohen, N. Dobrzynski, S. Senanayake, W. Xu and M. S. Whittingham, *Chem. Mater.,* 2013, **25**, 85.
7 N. Marx, L. Bourgeois, D. Carlier, A. Wattiaux, E. Suard, F. Le Cras and L. Croguennec, *Inorg. Chem*., 2012, **51**, 3146.
8 E. Palacios, P. Leret, J. F. Fernandez, A. H. De Aza and M. A. Rodriguez, *J. Nanopart. Res.,* 2012, **14**, 1131.
9 L. Croguennec and M. R. Palacin, *J. Am. Chem. Soc.,* 2015, **137**, 3140.
10 H. Tanaka, T. Okumiya, S. K. Ueda, Y. Taketani and M. Murakami, *Mater. Res. Bull.,* 2009, **44**, 328.
11 D. Yu, J. Qian, N. Xue, D. Zhang, C. Wang, X. Guo, W. Ding and Y. Chen, *Langmuir,* 2007, **23**, 382.

12 A. Mogus-Milankovic, D. E. Day, G. J. Long and G. K. Marasinghe, *Phys. Chem. Glasses,* 1996, **37**, 57.
13 L. Wang, C. V. Putnis, E. Ruiz-Agudo, J. Hoevelmann and A. Putnis, *Environ. Sci. Technol.,* 2015, **49**, 4184.
14 Y. Yin, H. Zhang, P. Wu, B. Zhou and C. Cai, *Nanotechnology,* 2010, **21**, 425504.
15 A. E. Jazouli, S. Benmokhtar, H. Belmal, J. P. Chaminade, P. Gravereau, S. Pechev, J. C. Grenier, G. Villeneuve and D. de Waal, *J. Solid State Chem.,* 2007, **180**, 772.
16 R. Lin, Y. Ding, L. Gong, W. Dong, J. Wang and T. Zhang, *J. Catal.,* 2010, **272**, 65.
17 X. Wang, Y. Wang, Q. Tang, Q. Guo, Q. Zhang and H. Wan, *J. Catal.,* 2003, **217**, 457.
18 E. Muneyama, A. Kunishige, K. Ohdan and M. Ai, *J. Catal.,* 1996, **158**, 378.
19 K. P. Singh, E. J. Bae and J. S. Yu, *J. Am. Chem. Soc.,* 2015, **137**, 3165.
20 P. Bonnet, J. M. M. Millet, C. Leclercq and J. C. Védrine, *J. Catal.,* 1996, **158**, 128.
21 A. Kahoul and A. Hammouche, *Ionics,* 2010, **16**, 105.
22 W. J. Cui, H. J. Liu, C. X. Wang and Y. Y. Xia, *Electrochem. Commun.,* 2008, **10**, 1587.
23 Y. N. Song, P. Y. Zavalij, M. Suzuki and M. S. Whittingham, *Inorg. Chem.,* 2002, **41**, 5778.
24 A. K. Padhi, K. S. Nanjundaswamy and J. B. Goodenough, *J. Electrochem. Soc.,* 1997, **144**, 1188.
25 N. Aliouane, T. Badeche, Y. Gagou, E. Nigrelli and P. Saint-Gregoire, *Ferroelectrics,* 2000, **241**, 255.
26 H. H. Chang, C. C. Chang, H. C. Wu, Z. Z. Guo, M. H. Yang, Y. P. Chiang, H. S. Sheu and N. L. Wu, *J. Power Sources,* 2006, **158**, 550.
27 K. Zaghib and C. M. Julien, *J. Power Sources,* 2005, **142**, 279.
28 C. Masquelier, P. Reale, C. Wurm, M. Morcrette, L. Dupont, D. Larcher, *J. Electrochem. Soc.*, 2002, **149**, A1037.
29 D. Karabelli, S. Unal, T. Shahwan and A. E. Eroglu, *Chem. Eng. J.,* 2011, **168**, 979.
30 G. K. Kouassi, *Curr. Nanosci*., 2011, **7**, 510.
31 N. Marx, L. Croguennec, D. Carlier, L. Bourgeois, P. Kubiak, F. Le Cras and C. Delmas, *Chem. Mater*., 2010, **22**, 1854.
32 X. Yang, S. M. Zhang, J. X. Zhang, M. Y. Xu, P. Ren, X. C. Li and L. C. Yan, *Funct. Mater. Lett*., 2011, **4**, 323.
33 M. Khachani, A. El Hamidi, M. Kacimi, M. Halim and S. Arsalane, *Thermochim. Acta,* 2015, **610**, 29.
34 H. Tanaka and K. Taniguchi, *Colloid Surf., A,* 2009, **334**, 165.
35 P. Reale, B. Scrosati, C. Delacourt, C. Wurm, M. Morcrette and C. Masquelier, *Chem. Mater*., 2003, **15**, 5051.
36 C. Luengo, M. Brigante, J. Antelo and M. Avena, *J. Colloid Interface Sci*., 2006, **300**, 511.
37 L. Li and R. Stanforth, *J. Colloid Interface Sci*., 2000, **230**, 12.
38 A. Ler and R. Stanforth, *Environ. Sci. Technol*., 2003, **37**, 2694.
39 S. Fendorf, M. J. Eick, P. Grossl and D. L. Sparks, *Environ. Sci. Technol*., 1997, **31**, 315.
40 A. Omoike, J. Chorover, K. D. Kwon and J. D. Kubicki, *Langmuir,* 2004, **20**, 11108.
41 R. G. Jonasson, R. R. Martin, M. E. Giuliacci and K. Tazaki, *J. Chem. Soc. Faraday Trans.,* 1988, **84**, 2311.
42 Z. F. Pu, M. H. Cao, Y. Jing, K. L. Huang and C. W. Hu, *Nanotechnology,* 2006, **17**, 799.
43 X. Wang, X. Y. Chen, L. S. Gao, H. G. Zheng, M. R. Ji, C. M.Tang, T. Shen and Z. D. Zhang, *J. Mater. Chem*., 2004, **14**, 905.
44 Y. Barbaux, M. Dekiouk, D. Lemaguer, L. Gengemere, D. Huchette and J. Grimblot, *Appl. Catal*., *A*, 1992, **90**, 51.
45 B. C. Sales, M. M. Abraham, J. B. Bates and L. A. Boatner, *J. Non-Cryst. Solids,* 1985, **71***,* 103.
46 C. Delacourt, P. Poizot, D. Bonnin and C. Masquelier, *J. Electrochem. Soc*., 2009, **156**, A595.
47 C. A. Barrero, K. E. Garcia, A. L. Morales, S. Kodjikian and J. M. Greneche, *J. Phys.: Condens. Matter,* 2006, **18**, 6827.
48 A. Kumar and S. K. Gupta, *J. Mater. Chem. B,* 2013, **1**, 5818.

Supplementary information

Phase-controlled synthesis of iron phosphates via phosphation of β-FeOOH nanorods

Ronghe Lin,[a] Amol P. Amrute,[a] Frank Krumeich,[b] Károly Lázár,[c] Roland Hauert,[d] Maxim Yulikov[e] and Javier Pérez-Ramírez*[a]

[a.] *Institute for Chemical and Bioengineering, Department of Chemistry and Applied Biosciences, ETH Zurich, Vladimir-Prelog-Weg 1, CH-8093 Zurich, Switzerland. Email: jpr@chem.ethz.ch*

[b.] *Laboratory of Inorganic Chemistry, Department of Chemistry and Applied Biosciences, ETH Zurich, Vladimir-Prelog-Weg 1, CH-8093 Zurich, Switzerland.*

[c.] *Department of Nuclear Analysis, Center for Energy Research, MTA, Konkoly-Thege M. 29-33, H-1121 Budapest, Hungary.*

[d.] *Empa, Swiss Federal Laboratories for Materials Science and Technology, Überlandstrasse 129, CH-8600 Dübendorf, Switzerland.*

[e.] *Laboratory of Physical Chemistry, Department of Chemistry and Applied Biosciences, ETH Zurich, Vladimir-Prelog-Weg 2, CH-8093 Zurich, Switzerland.*

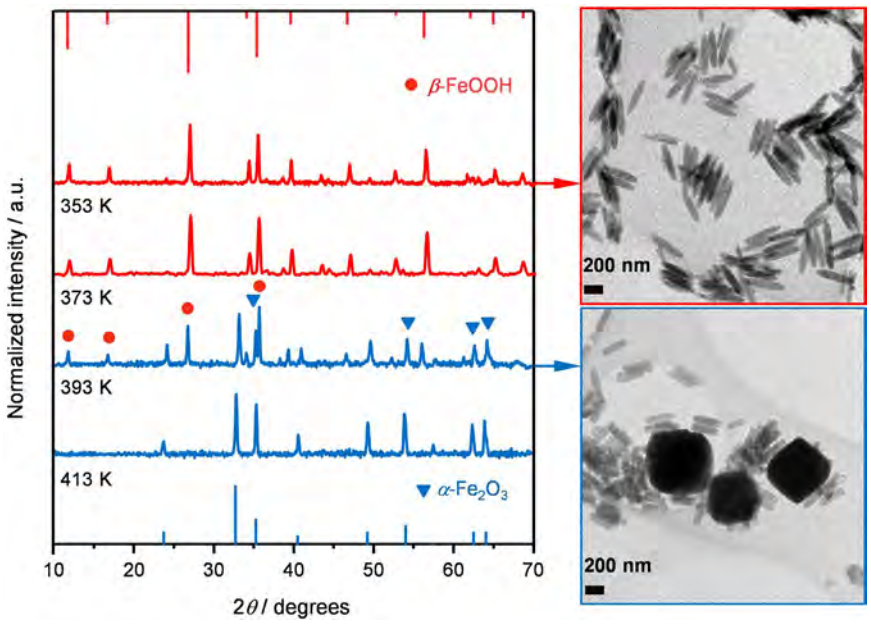

Fig. S1. Synthesis of β-FeOOH nanorods by hydrolysis of $FeCl_3$. X-ray powder diffractograms and corresponding TEM images of the synthesised samples at different hydrothermal temperatures. Vertical lines on the top and bottom axes correspond to the reference β-FeOOH (JCPDS 34-1266) and α-Fe_2O_3 (JCPDS 33-0664), respectively.

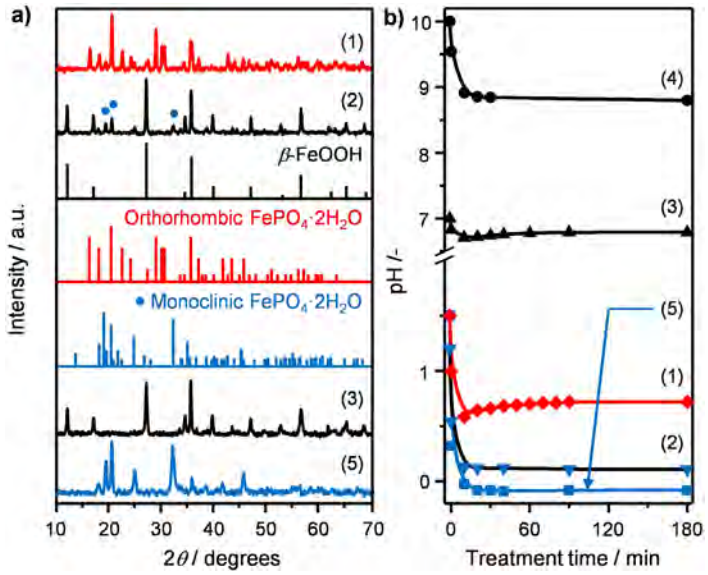

Fig. S2. Influence of pH (1-4) and iron precursor (5) on the formation of $FePO_4{\cdot}2H_2O$ *via* treatment of β-FeOOH-nr (1-4) or $Fe(NO_3)_3$ with H_3PO_4 at P/Fe = 1.8 and 353 K for 3 h (14 h for $Fe(NO_3)_3$ as no precipitate was formed in 3 h). **a**) XRD patterns of the solid samples and **b**) pH evolution as a function of time. (1) pH 1.5 (β-FeOOH/H_3PO_4); (2) pH 1.2 (β-FeOOH/H_3PO_4/HNO_3, this pH value is equal to that of the treatment solution with P/Fe = 8.9); (3) pH 7 (β-FeOOH/H_3PO_4/$NH_3{\cdot}H_2O$); (4) pH 10 (β-FeOOH/H_3PO_4/$NH_3{\cdot}H_2O$); (5) pH 1.5 ($Fe(NO_3)_3$/H_3PO_4), 14 h. Vertical lines in **a**) show the reference orthorhombic (JCPDS 33-667) and monoclinic (JCPDS 33-666) $FePO_4{\cdot}2H_2O$, and β-FeOOH (JCPDS 34-1266).

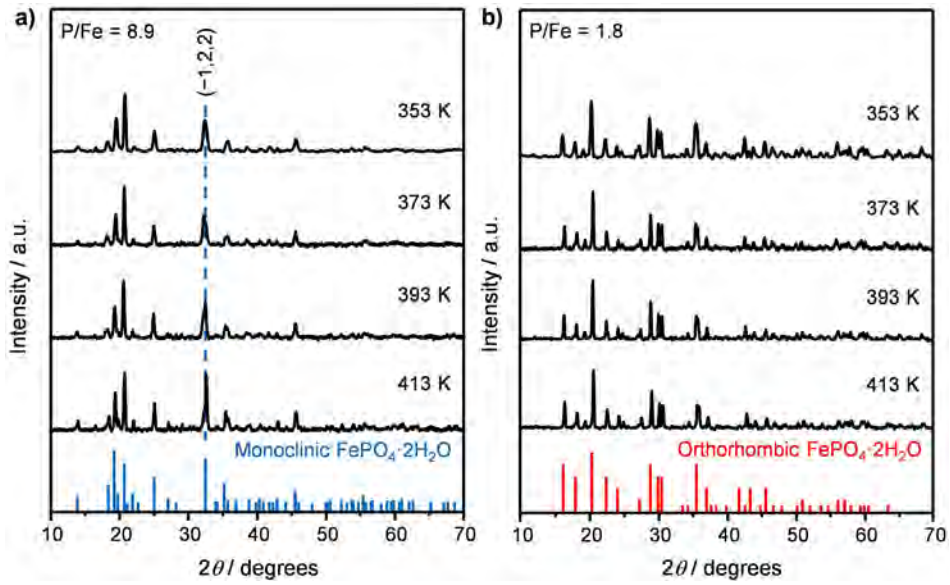

Fig. S3. XRD patterns of samples obtained *via* phosphation of β-FeOOH-nr with H_3PO_4 for 14 h at different temperatures. **a**) P/Fe = 8.9 and **b**) P/Fe = 1.8. Vertical lines on the bottom axes belong to the reference orthorhombic (JCPDS 33-667) and monoclinic (JCPDS 33-666) $FePO_4 \cdot 2H_2O$. The patterns in **a**) indicate the preferential orientation of monoclinic $FePO_4 \cdot 2H_2O$ in the (−1,2,2) direction at $2\theta = 32.17°$ at higher treatment temperatures.

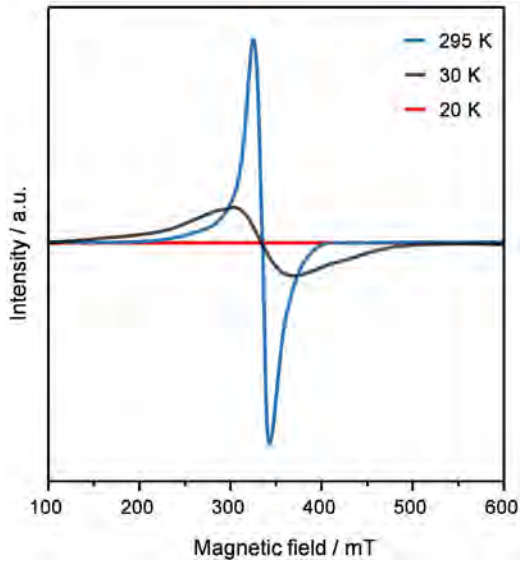

Fig. S4. EPR spectra of $FePO_4$ (derived by calcination of the M-14 sample at 923 K for 5 h) recorded at different temperatures. The EPR line disappears at 20 K, in accordance with the known antiferromagnetic transition of $FePO_4$. Note that the room-temperature spectra were measured with a resonant frequency of 9.886 GHz. The low-temperature spectra were measured with a cryostat tube inserted into the resonator, which shifted the resonance frequency to 9.485 GHz. The room-temperature spectrum was shifted accordingly to adjust the frequency difference. These results confirm that the EPR signals observed in the M-*t* and O-*t* samples are due to the formation of iron phosphates.

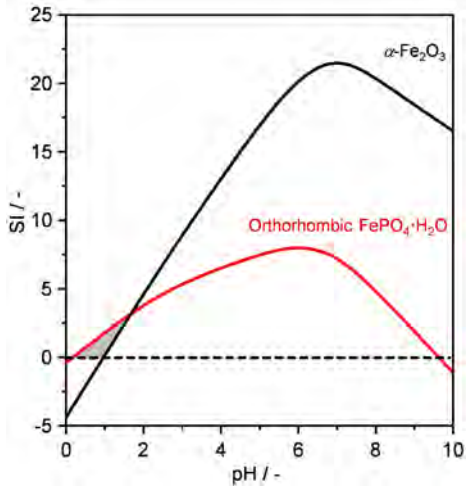

Fig. S5. Saturation index (SI) of orthorhombic $FePO_4 \cdot 2H_2O$ and α-Fe_2O_3 as a function of pH during the phosphation of β-FeOOH-nr with H_3PO_4 at P/Fe = 1.8. The dissolved iron was set as 30 mg Fe g^{-1} β-FeOOH, which was the maximum amount detected by AAS. The influence of other anions on the pH adjustment was not considered. Calculations of SI values were performed using the Visual MINTEQ software. The gray area highlights the narrow pH range in which the formation of orthorhombic $FePO_4 \cdot 2H_2O$ is favorable. The SI of monoclinic $FePO_4 \cdot 2H_2O$ was not calculated due to the unavailability of thermodynamic parameters.

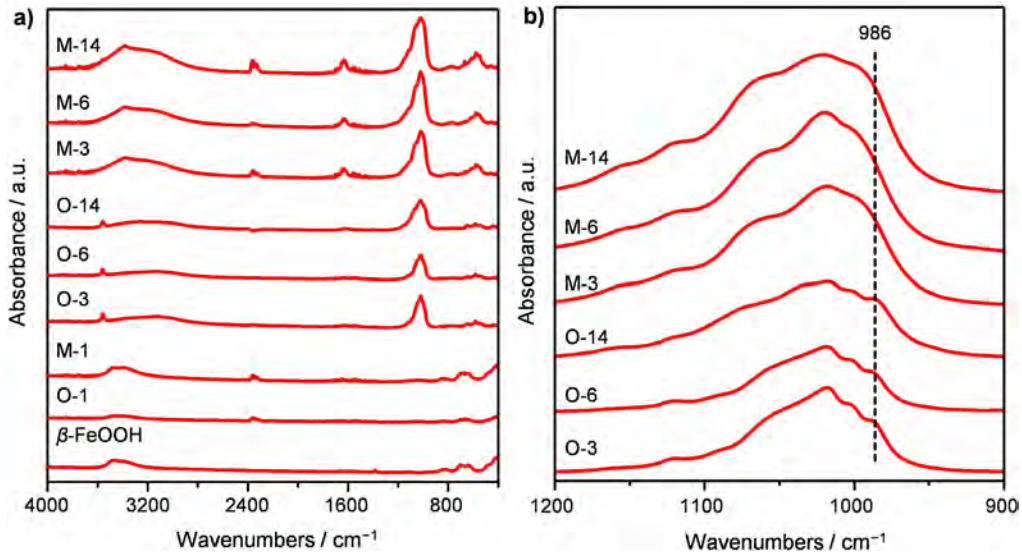

Fig. S6. a) FTIR spectra of β-FeOOH-nr and the samples derived from treatment in H_3PO_4. **b**) Enlargement of the range of 900-1200 cm^{-1}, showing the vibrational modes of the phosphate groups in M-*t* and O-*t* samples. Nominal atomic ratios of the M-*t* and O-*t* samples were **a**) P/Fe = 8.9 and **b**) P/Fe = 1.8 respectively, where *t* denotes the treatment time in hours. Among the broad envelop of bands at 950-1100 cm^{-1}, a shoulder at 986 nm^{-1} was observed only for the O-*t* samples. This suggests that at least one extra surface complex was formed during the formation of orthorhombic $FePO_4 \cdot 2H_2O$.

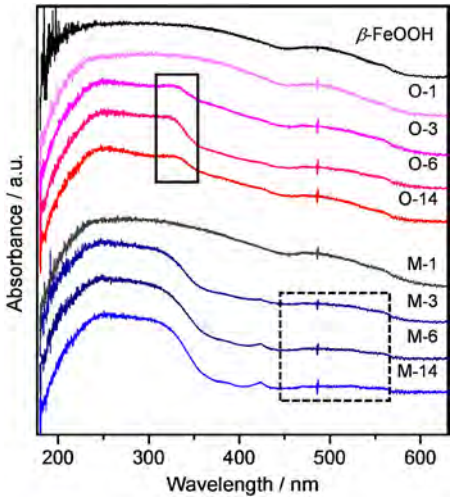

Fig. S7. UV-Vis spectra of β-FeOOH-nr and the samples derived from treatment in H_3PO_4. After 3 h of treatment, the absorption in the visible range virtually disappeared for M-*t* samples as indicated by the dashed box, while a shoulder emerged at *ca.* 320 nm for the O-*t* samples (solid box). These observations further demonstrate that different interactions may occur between β-FeOOH-nr and H_3PO_4 during the formation of different phases of $FePO_4{\cdot}2H_2O$.

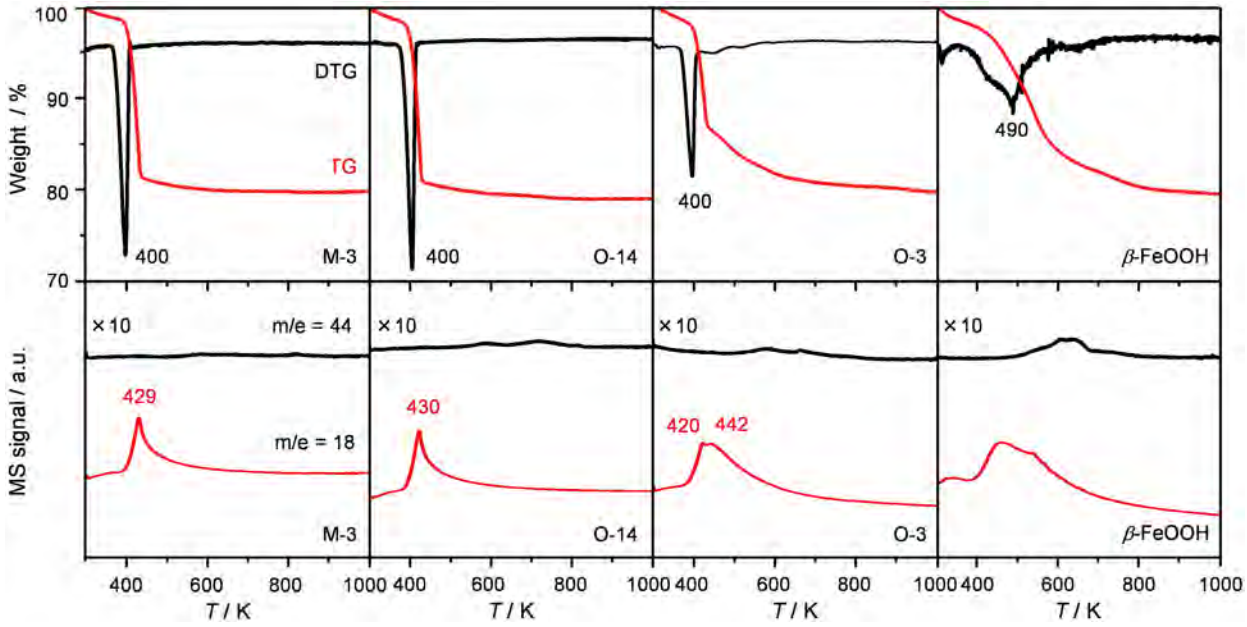

Fig. S8. TGA-MS profiles of monoclinic (M-3) and orthorhombic (O-14) $FePO_4{\cdot}2H_2O$, O-3, and β-FeOOH-nr.

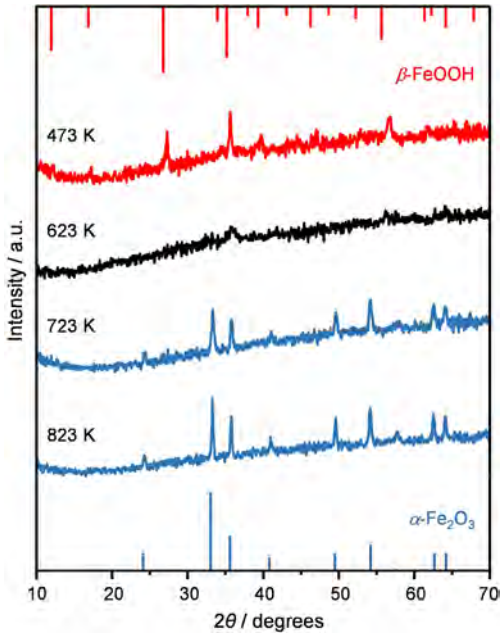

Fig. S9. XRD patterns of β-FeOOH-nr after calcination for 5 h at different temperatures. Vertical lines on the top and bottom axes are the reference β-FeOOH (JCPDS 34-1266) and α-Fe_2O_3 (JCPDS 33-0664).

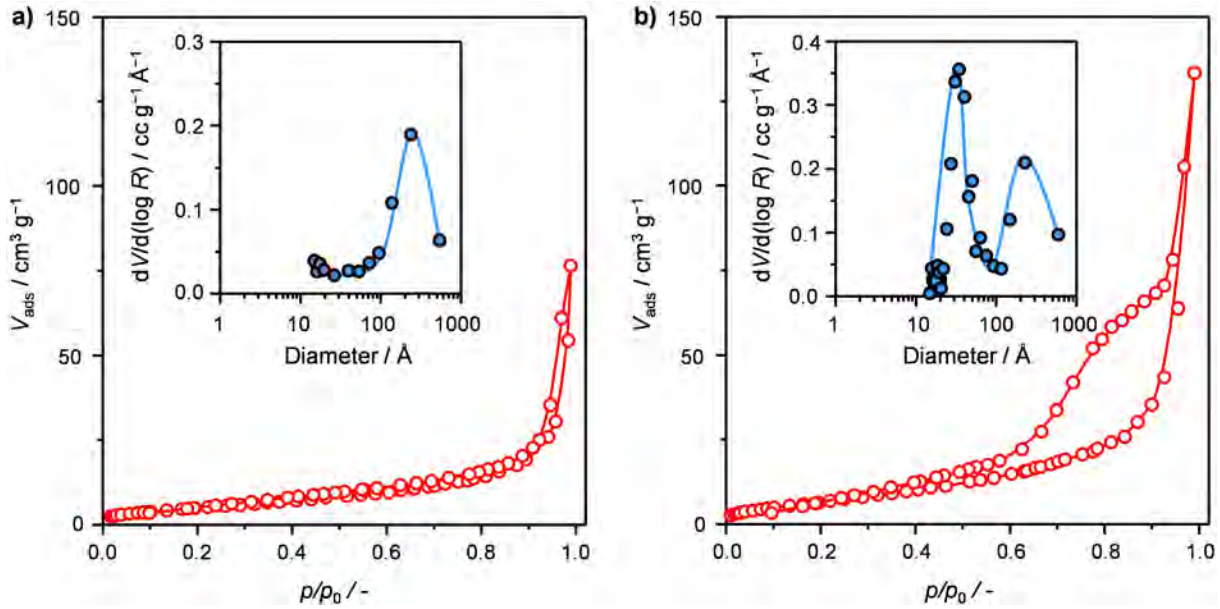

Fig. S10. N_2 sorption isotherms of the **a**) β-FeOOH-nr and **b**) O-3 samples after calcination at 923 K for 5 h. Inset: pore size distribution derived by the BJH method using the desorption branch.